instruments

Technical Note

Critical-Angle Differential Refractometry of Lossy Media: A Theoretical Study and Practical Design Issues

Spyridon Koutsoumpos, Panagiotis Giannios †, Dimos Triantis and Konstantinos Moutzouris *

Electronic Devices & Materials Lab, Department of Electrical & Electronic Engineering, University of West Attica, 12243 Athens, Greece

* Correspondence: moutzouris@uniwa.gr; Tel.: +30-210-538-1306

† Current address: Barcelona Institute of Science and Technology, Institute for Research in Biomedicine, IRB Barcelona 08028, Spain.

Received: 3 June 2019; Accepted: 30 July 2019; Published: 31 July 2019

Abstract: At a critical angle of incidence, Fresnel reflectance at an interface between a front transparent and a rear lossy medium exhibits sensitive dependencies on the complex refractive index of the latter. This effect facilitates the design of optical sensors exploiting single (or multiple) reflections inside a prism (or a parallel plate). We determine an empirical framework that captures performance specifications of this sensing scheme, including sensitivity, detection limit, range of linearity and—what we define here as—angular acceptance bandwidth. Subsequently, we develop an optimization protocol that accounts for all relevant optical or geometrical variables and that can be utilized in any application.

Keywords: optical sensors; biological and chemical sensing; refractometry; total internal reflection

1. Introduction

Refractive index sensors are intensely investigated for numerous biomedical [1–3], chemical [4,5] and industrial [6,7] applications. An indicative yet far from exhaustive list of sensing mechanisms relies on plasmonic [8–11], photonic crystal [12–15], micro-cavity [16–19], optical fiber [20–23] and wave-guide [24–27] configurations. Associated with Fresnel reflectance properties at planar interfaces, differential refractometry offers an alternative path to sensing refractive index changes, by exploitation of interference [28], deflection [29] or (more relevant to the present work) critical-angle [30–35] effects. Today, differential refractometry is not only a standard analytical tool that operates routinely in many laboratories, but also infiltrates emerging optofluidic and lab-on-chip technologies [36–38].

In critical-angle differential refractometry (CADR), a front transparent medium (commonly, a prism) is interfaced with a sample which, typically, is also assumed to be lossless. The underlying principle of operation is simple: provided that the front medium is optically denser than the sample, there exists a sharp transition from total internal reflection (TIR) to partial internal reflection, taking place at a critical angle which corresponds to the location of an abrupt discontinuity in the derivative of reflectance with respect to incidence angle. Operating the sensing interface at the transition point leads to the generation of an intensity readout signal, as soon as the TIR condition is disturbed by refractive index fluctuations.

With non-transparent samples, CADR interpretation is less straightforward. To begin with, the refractive index of the rear medium becomes a complex quantity, the imaginary part of which incorporates absorption or scattering effects. Furthermore, reflectance never reaches unity (except for the limiting case of incidence at 90° with respect to the surface normal) and the transition from "attenuated" total internal reflection (ATIR) to partial internal reflection is gradual. As a result, the reflectance derivative with respect to incidence angle, now peaking to a finite value, is no longer the proper quantity to conceptualize the sensing principle; this purpose is better served by reflectance derivatives with respect to the real and imaginary index of the sample. These are negative quantities exhibiting local extrema at the vicinity of the transition from ATIR to partial internal reflection, albeit at slightly different "critical" angles. In general, these extrema are stronger for p- than for s-polarization, an observation that indicates the preferential wave orientation for CADR sensing.

In this work, we attempt a theoretical study of CADR with lossy media, accounting for (i) the standard prism configuration, (ii) an alternative geometry that exploits multiple reflections inside a parallel plate. Both schemes are, in principle, compatible with optofluidic technologies and static or real-time monitoring applications. We untangle the perplex dependencies of the sensor's specifications on various optical and geometrical parameters, revealing among other facts the dominant role of the sample's loss. In doing so, we introduce the concept of the "angular acceptance bandwidth" which trades-off with sensor's sensitivity and helps clarify several complexities in terms of light coupling and detection. Our results provide a universal roadmap for rapid performance evaluation and optimization of CADR devices, which might be essential for pushing the technique's detection limit from the current standard ($\sim$ 100 µRIU) down to the current state-of-the-art ($\sim$ 1 µRIU for CADR [31], as well as for all noninterferometric methods), or even lower.

2. Theoretical Background

The isosceles triangular prism and parallelogram plate configurations under investigation are depicted in Figure 1. The sample is interfaced with the base of the prism, or equivalently, the top side of the plate, the bottom of which is high-reflection-coated. Coming from air, light hits the input facet at an external angle of incidence θ and reaches the output facet at an angle ϕ, after $N = 1$ (or $N > 1$) reflections at the sensing interface of the prism (plate), respectively; each one of these reflections is at a constant angle θ_1. The input and output coupling geometries are determined by the cut angle α, which in Figure 1 is taken $\alpha < \pi/2$; however, the upcoming formalism remains valid also for $\alpha \geq \pi/2$. Then, θ, ϕ and θ_1 (which are trivially defined with respect to the corresponding normal), as well as plate's length L and thickness d (which is assumed to be much larger than the light wavelength, so as to avoid interference effects), relate via:

$$\theta_1 = \alpha - \phi, \quad \phi = arcsin\left[\frac{n_{air}}{n_o} \cdot sin\theta\right], \quad L \approx 2d \cdot N \cdot tan(\theta_1) \tag{1}$$

where $n_{air}(\approx 1)$ and n_o are the real indices of air and the transparent prism (or plate), respectively.

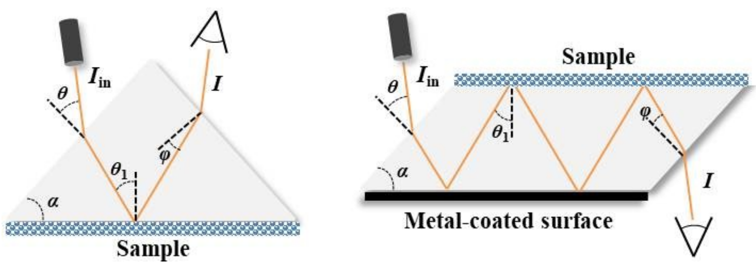

Figure 1. Prism (**left**) and parallel plate (**right**) configurations, the latter shown $N = 2$ reflections at the sensing interface.

Light transfer in the proposed layouts can be accurately simulated via standard Fresnel theory. Let us begin by assuming that a reference medium with a complex refractive index $(n = n_r - in_i)$ is first put to the test. The "reference" prim/plate transmittance T_p, defined as the ratio of the output light intensity I_{ref} over incident light intensity I_{in}, is:

$$T_p(\theta) = \frac{I_{ref}}{I_{in}} = \left[1 - R_{1/2}(\theta)\right] \cdot \left[R_{2/3}(\theta_1)\right]^N \cdot \left[1 - R_{2/1}(\phi)\right] \tag{2}$$

where $R_{k/j}$ is the reflectance at the interface between medium k and medium j ($k, j = 1, 2, 3$ with $1 = air$, $2 = prism/plate$, $3 = sample$); Reflectance at the metal-coated surface of the plate is taken as unity; Equation (2) is valid for the prism, as well as the plate, by proper substitution of the respective N value. In turn, $R_{k/j}$ is the squared modulus of the corresponding Fresnel amplitude coefficient, which—for the preferred p-polarization—reads:

$$r_{k/j}(\angle) = \frac{cos(\angle) \cdot (n_j/n_k)^2 - \sqrt{(n_j/n_k)^2 - sin^2(\angle)}}{cos(\angle) \cdot (n_j/n_k)^2 + \sqrt{(n_j/n_k)^2 - sin^2(\angle)}} \tag{3}$$

where $\angle = \theta, \theta_1, \phi$ for $(k/j = 1/2,\ 2/3,\ 2/1)$ and n_k, n_j are the refractive indices of the respective media.

Then, suppose that the reference medium is replaced by a corrupted sample, which exhibits a complex index

$$n' = (n_r + \delta n_r) - i \cdot (n_i + \delta n_i) = n + (\delta n_r - i \cdot \delta n_i) \tag{4}$$

that is, equal to the refractive index n of the reference medium, with an added perturbation term that comprises a real (δn_r) and an imaginary (δn_i) component. At this point, we may appropriately define a total index perturbation parameter δ via:

$$\delta = \delta n_r + \delta n_i. \tag{5}$$

This index perturbation term shifts the plate transmittance (and output intensity) to new values T (and I) that can be straightforwardly calculated by substituting n' for n in Equation (2). Assuming that the incident light intensity I_{in} remains constant, the relative intensity change $\Delta I/I$ between measurements of the corrupted and reference sample is:

$$\frac{\Delta I}{I} = \frac{I - I_{ref}}{I} = \frac{T - T_p}{T} \tag{6}$$

Figure 2 depicts the reference transmittance T_p, along with the relative intensity change $\Delta I/I$, versus external angle of incidence θ; specifics on parameters used for calculations are given in the figure's label. (Note that the assumption of unit reflectance at the metal-coated surface may lead to somewhat overestimated T_p values, but does not affect the relative intensity change.) Apparently, $\Delta I/I$ exhibits local extremum at a critical external angle $\theta = \theta_c$, which shifts only slightly, when a perturbation in the real index alone ($\delta = \delta n_r$) is replaced by an equal-sized perturbation in the imaginary index ($\delta = \delta n_i$). Interestingly, these two cases are distinguishable by the asymmetric shape of the relative intensity change curve; indeed, when $\delta = \delta n_r$ ($\delta = \delta n_i$), $\Delta I/I$ decays faster towards smaller (larger) incidence angles, respectively. These observations reflect similar properties of the reflectance derivatives with respect to n_r, n_i and may be relevant for applications requiring sensor's selectivity.

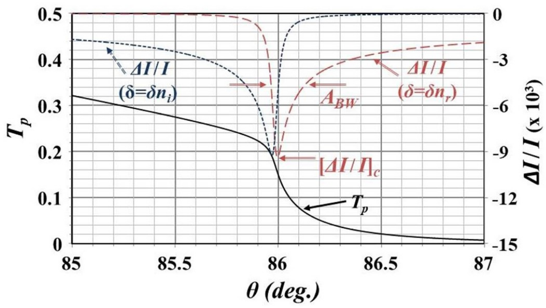

Figure 2. Transmittance T_p (solid line) and relative intensity change $\Delta I/I$ for $\delta = \delta n_r = 1$ µRIU (dashed line) and $\delta = \delta n_i = 1$ µRIU (dotted line), versus incidence angle θ. Calculations assume $n_r/n_0 = 0.75$, $n_i/n_0 = 10^{-5}$, $N = 12$, $\alpha = 76.1°$, $n_o = 2.16$, $n_{air} = 1$.

3. Signal, Sensitivity and Acceptance Bandwidth

From a practical standpoint, the most important features of the relative intensity change curve are (i) its extreme value at the critical angle $\left[\Delta I/I\right]_c$, thereon understood as the sensor's output signal, (ii) its angular bandwidth A_{BW}, defined as the full-width-at-half-maximum and thereon understood as the sensor's acceptance bandwidth. Due to the entangled dependencies on multiple variables, attempting to evaluate the sensor's signal and acceptance bandwidth by generating successive plots like those presented in Figure 2, is an elaborate, time-demanding and somewhat confusing task. Fortunately, we found out that it is possible to produce a set of empirical equations that can handily trace both $\left[\Delta I/I\right]_c$ and A_{BW} (more details on the heuristic model-building process are given in Appendix A). These equations are:

$$\left[\frac{\Delta I}{I}\right]_c = S \cdot \delta \tag{7}$$

$$S \approx -F(n_r/n_o) \cdot \left(\frac{n_i}{n_o}\right)^{-a_o} \cdot \left(\frac{N}{n_o}\right) \cdot \delta_1, \tag{8}$$

$$A_{BW} \approx 10^5 \cdot \left[\left.\frac{d\theta_1}{d\theta}\right|_{\theta=\theta_c}\right]^{-1} \cdot G(n_r/n_o) \cdot \left(\frac{n_i}{n_o}\right) \cdot \delta_2, \tag{9}$$

where S is sensor's sensitivity, A_{BW} is given in degrees and:

$$\delta_1 = 1 - \frac{1}{2}\frac{\delta n_r}{\delta} + \frac{1}{2}\left(\frac{\delta n_r}{\delta}\right)^2,\ \delta_2 = 1 - \frac{\delta n_r}{\delta} + \left(\frac{\delta n_r}{\delta}\right)^2 \tag{10}$$

are factors acquiring a maximum value of 1 when $\delta = \delta n_r + \delta n_i = \delta n_r$ or $\delta = \delta n_r + \delta n_i = \delta n_i$, and a minimum value when $\delta n_r = \delta n_i = \delta/2$,

$$F(n_r/n_o) = a_1 \cdot exp\left[a_2\left(\frac{n_r}{n_o}\right)^{-1}\right] + a_3\left[1 - a_4\left(\frac{n_r}{n_o}\right)\right]^{-1}, \tag{11}$$

$$G(n_r/n_o) = a_5 + a_6 \cdot \left[1 - a_7\left(\frac{n_r}{n_o}\right)\right]^{-1/2}, \tag{12}$$

and

$$\left.\frac{d\theta_1}{d\theta}\right|_{\theta=\theta_c} = cos\theta_c \cdot \left[\left(\frac{n_{air}}{n_o}\right)^{-2} - sin^2\theta_c\right]^{-1/2}, \tag{13}$$

with: $a_o = 0.49458$, $a_1 = 1.84$, $a_2 = 0.695658$, $a_3 = 0.267344$, $a_4 = 0.990367$, $a_5 = 0.000717133$, $a_6 = 0.00259023$, $a_7 = 1.00072$.

Equations (7)–(9) reproduce the sensor's signal, sensitivity and acceptance bandwidth with a typical accuracy of second significant digit, which is sufficient for evaluation and optimization purposes, as long as the respective variables remain within the following ranges:

$$\delta < n_i, \;\; N < 50, \;\; 0.5 < \frac{n_r}{n_o} < 1, \;\; 10^{-2} < \frac{n_i}{n_o} < 10^{-8}, \tag{14}$$

The information contained in these empirical equations is graphically exposed in Figure 3. Therein, it is clear that $\left[\Delta I/I\right]_c$ depends explicitly on δ, $\delta n_r/\delta$, N/n_o, n_r/n_o and n_i/n_o. These dependencies are linear with respect to δ and N/n_o, but nonlinear with respect to the remaining three variables, such that the signal maximizes when: $\delta n_r/\delta = 0 \; or \; 1$, $n_r/n_o \to 1$ and, more rapidly, as n_i/n_o reduces. It is noted that sensitivity S is by definition a direct measure of the output signal—after normalization by the input stimuli δ—and thus, it behaves likewise.

Comparatively, A_{BW} exhibits nonlinear dependencies on $\delta n_r/\delta$, n_r/n_o and scales linearly with n_i/n_o; however, it is not affected by δ or N. Contrary to $\left[\Delta I/I\right]_c$, which is geometry-independent, A_{BW} varies also with the critical angle θ_c. This nonlinear dependence emerges from the derivative $d\theta_1/d\theta|_{\theta=\theta_c}$, which translates the internal angular bandwidth (in terms of θ_1) into an external one (in terms of θ). Note that the critical angle θ_c is tunable by means of the plate's angle α, as is indicated by Equation (1). Derivative $d\theta_1/d\theta|_{\theta=\theta_c}$ introduces also a relatively weak dependence on n_{air}/n_o, which can be neglected at first instance and, thus, is not included in Figure 3. To sum up, angular acceptance bandwidth maximizes when: $\delta n_r/\delta = 0 \; or \; 1$, $n_r/n_o \to 1$, $\theta_c \to 90°$ and, more rapidly, as n_i/n_o increases.

Remarkably, the main regulator of the sensor's sensitivity (or equivalently, signal) and acceptance bandwidth is the sample's imaginary index, which introduces a trade-off between these quantities. Indeed, at the limit of transparency ($n_i = 0$) Equations (8) and (9) return an infinite S and a null A_{BW}; this result conforms with the standard CARD interpretation, conveying features of the reflectance derivative with respect to incidence angle, at the point of discontinuity. Inversely, as loss increases, sensitivity tends to zero and acceptance bandwidth grows larger.

The only means available for simultaneous increase in S and A_{BW}, which is an obvious-seeming operational advantage, is to stretch parameters $\{n_r/n_o, \; N, \; \theta_c\}$ close to their limiting values $\{1, \; \gg \; 1, \; 90°\}$. Although appealing in principle, these limits should be avoided in practise, because they diminish the overall prism/plate transmittance, an effect that intensifies with increasing loss and complicates output light detection. There exists two more reasons to avoid $N \gg 1$. First, large N values deteriorate sensor's performance if the plate is not perfectly parallel, a repercussion that is otherwise minor, considering the sub-μrad tolerances that are nowadays available with state-of-the-art plane-parallel optics. Second, $N \gg 1$ corresponds to large plate lengths, compromising the device's compactness and increasing sample volume demands.

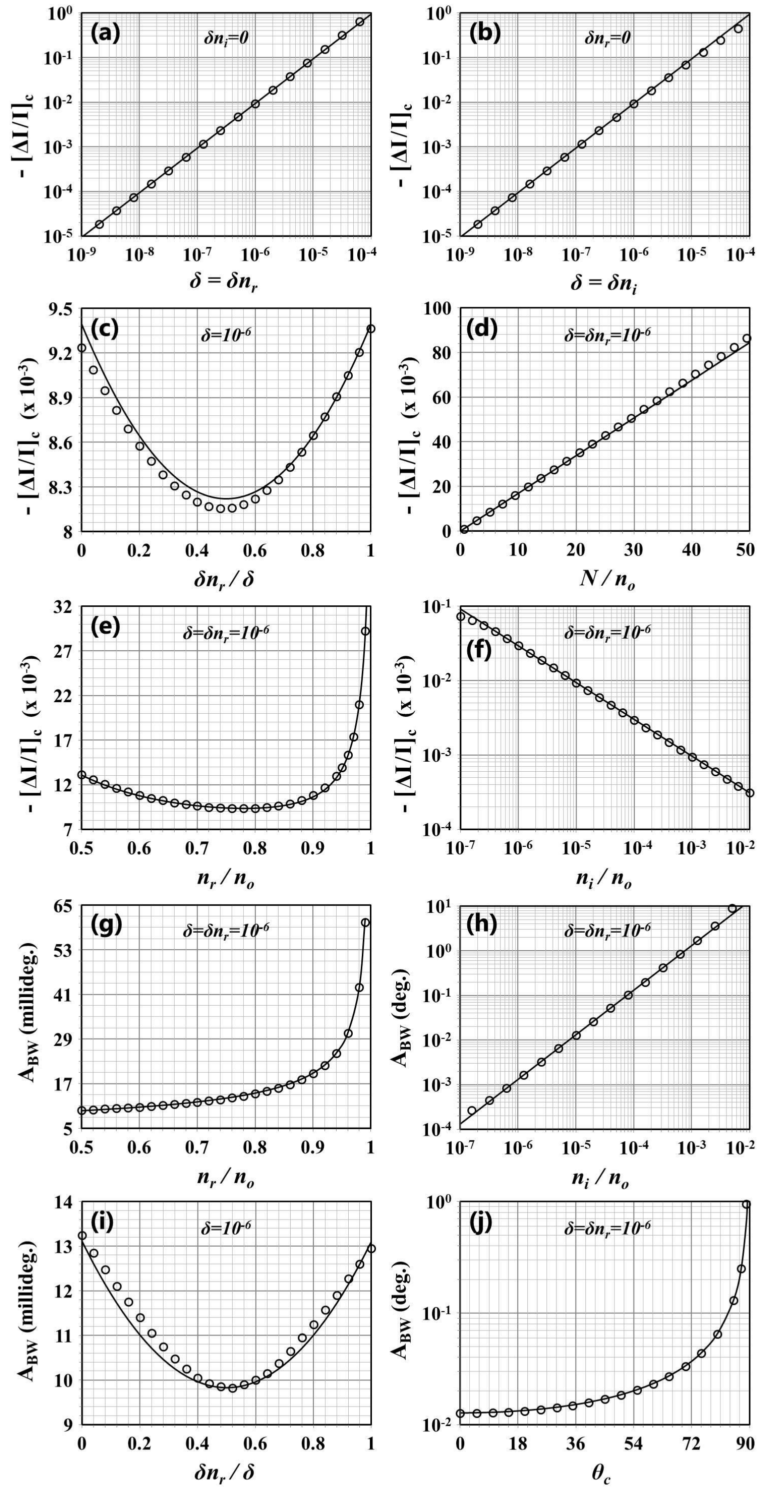

Figure 3. Output signal $[\Delta I/I]_c$ and angular acceptance bandwidth A_{BW}, as a function of relevant variables. Open circles correspond to exact values derived from signal-versus-incidence-angle plots, by use of Equations (2) and (6); solid lines are estimates from the empirical Equations (7) and (9). Throughout, values of parameters other than x-axis variables are: $n_{air} = 1$, $n_r/n_o = 0.75$, $n_i/n_o = 10^{-5}$, $N/n_o = 1/0.18$. Specifics on the index perturbation values δ, δn_r and δn_i are provided in each individual plot. A_{BW} calculations assumed $n_o = 2.16$; the angle α was properly varied to maintain a constant $\theta_c = 15°$ in (**g**), (**h**,**i**), but a properly scalable θ_c in (**j**). Respective values for $[\Delta I/I]_c$ calculations are irrelevant, since they do not affect the results, but are reported for the sake of completeness: $n_o = 1.8$ and $\alpha = 81°$.

4. Detection Limit Considerations

The trade-off between sensitivity and angular acceptance bandwidth raises some interesting questions; does an optimal value for n_i and by extension, a preferred wavelength of operation, exist? If so, how can it be determined? The compromise solution to these problems emerges via detection limit (DL) considerations.

The detection limit, i.e., the minimum index perturbation that can be reliably sensed, is an instrument, and application-specific quantity that can be estimated, provided that significant sources of noise are distinguishable. For example, let us assume that non-negligible noise contributions originate from (i) the detection stage (σ_{det}), (ii) power fluctuations of the laser source (σ_{laser}), (iii) random fluctuations in the real index of the sample, caused by temperature instabilities ΔT and the nonzero spectral bandwidth $\Delta\lambda$ of the laser source, which introduce noise variance components $\sigma_T = S \cdot [dn_r/dT] \cdot \Delta T$ and $\sigma_\lambda = S \cdot [dn_r/d\lambda] \cdot \Delta\lambda$, respectively. These assumptions are reasonable, as long as the thermooptic and dispersion coefficients for the real index of the sample (i.e., dn_r/dT and $dn_r/d\lambda$) are much larger than the respective coefficients for n_i, n_o, and n_{air}.

Then, we may adopt standard convention $DL = 3\sigma/S$, where $\sigma \approx \sqrt{\sigma^2_{laser} + \sigma^2_T + \sigma^2_\lambda + \sigma^2_{det}}$ is the total noise variance, so as to deduce the following useful approximation:

$$DL \approx 3\sqrt{\sigma^2_{laser} + \left[S\,\frac{dn_r}{dT}\,\Delta T\right]^2 + \left[S\,\frac{dn_r}{d\lambda}\,\Delta\lambda\right]^2 + \sigma^2_{det}}\Big/ S. \tag{15}$$

It is appropriate at this point to parenthetically note that Equation (15) combined with the "rule of the thumb" articulated in Equation (14), specify the range of sensor's linear response, which is the last remaining major specification that depends also on sample's loss:

$$Linear\ \ range:\ DL < \delta < n_i. \tag{16}$$

Under the assumptions validating Equation (15), the detection limit decreases monotonically with increasing sensitivity, reaching its minimum theoretical value DL_{min} at the transparency limit (that is, where $S \to \infty$):

$$DL_{min} = \lim_{S\to\infty} DL = 3\sqrt{\left[\frac{dn_r}{dT}\,\Delta T\right]^2 + \left[\frac{dn_r}{d\lambda}\,\Delta\lambda\right]^2} \tag{17}$$

However, reduction in the detection limit by means of sensitivity increase is meaningful only up to the point that $S = S_{opt}$, where

$$S_{opt} = \sqrt{\frac{\sigma^2_{laser} + \sigma^2_{det}}{\left[\left(dn_r/dT\right)\,\Delta T\right]^2 + \left[\left(dn_r/d\lambda\right)\,\Delta\lambda\right]^2}}. \tag{18}$$

Indeed, when $S = S_{opt}$, the detection limit reaches its "optimum" value DL_{opt} that is equal to:

$$DL_{opt} = \sqrt{2}\,DL_{min} = 3\,\sqrt{2}\sqrt{\left[\frac{dn_r}{dT}\,\Delta T\right]^2 + \left[\frac{dn_r}{d\lambda}\,\Delta\lambda\right]^2}. \tag{19}$$

Further increase in sensitivity towards infinity (by decreasing n_i towards the transparency limit) has a negligible effect on DL, while drastically reducing the acceptance bandwidth. Besides, higher sensitivities also compromise sensor's range of linearity, as may be seen by inspection of Equation (15). Therefore, operating the sensing interface with $S > S_{opt}$ is not only unnecessary but also detrimental.

5. Spatially-Unresolved vs. Spatially-Resolved Detection

Setting $S = S_{opt}$ by choosing the proper value for n_i automatically locks angular acceptance bandwidth to its own respective value, which is easily determinable, as well as decisive for the design of the detection stage. The latter can be based either on a spatially-unresolved, or on a spatially-resolved, scheme.

Accurate spatially-unresolved detection (SUD) by use of a standard photodiode is the most straightforward option; it requires that the input light is stably coupled into the prism/plate at the critical angle θ_c, with its entire optical power contained within an angular spread that does not exceed A_{BW}. Assuming an input beam with high pointing-stability, waist radius w_o and quality factor M^2, the full-angle divergence θ_d at the diffraction-limit is:

$$\theta_d = \frac{2M^2\lambda}{\pi w_o} \tag{20}$$

and the implied condition for SUD detection reads:

$$SUD\ \ condition: \ \frac{A_{BW}}{\theta_d} \geq 1. \tag{21}$$

As A_{BW} becomes narrower (i.e., S_{opt} increases), the SUD condition necessitates beams with large waists. When Equation (21) is not fulfilled, the signal hides inside a fraction of the beam profile and, hence, spatially-resolved detection (SRD) by use of a diode array should be opted. Accurate SRD requires that the "active area" of the output beam profile (i.e., the fraction containing the sensing information) should be larger than the surface of at least one pixel of the diode array, that is:

$$SRD\ \ condition: \ \frac{d_{pixel}}{2w} < \frac{A_{BW}}{\theta_d}, \tag{22}$$

where d_{pixel} is the pixel's diameter and w is the beam radius at the detector.

When either of these conditions is fulfilled, detection noise may become negligible and thus, it is eliminated from Equation (15) and (18). Indeed, removing measurement complications associated with the finite acceptance bandwidth can reduce σ_{det} down to levels that relate only to fundamental noise mechanism, such as thermal and quantum noise. Then, we may reasonably assume that (i) the noise-equivalent-power at the photodiode will be in the sub-nW range, (ii) output light power reaching the detector will far exceed $\sim 1\ \mu W$. These assumptions confirm the estimate that $\sigma_{det} \ll 10^{-3}$, which is indeed well-below the power noise σ_{laser} of common laser sources.

6. Optimization Protocol

Following the preceding analysis, it is now possible to formulate a simple optimization process that can be always adopted, as long as the optical constants of the reference sample (i.e., n_r, n_i, dn_r/dT, $dn_r/d\lambda$) and their wavelength dependence are known. For the sake of simplicity, we may select $\delta_1 = \delta_2 = 1$, since in most practical cases an extraneous stimulus will affect primarily either the real or the imaginary index of the sample. The proposed protocol comprises the following steps:

Step 1: Impose strict temperature regulation and narrow-band laser emission (or spectral filtering), so as to reduce ΔT and $\Delta\lambda$; for any given sample, these are the only free variables affecting the detection limit, which can be calculated by use of Equation (19).

Step 2: Compute the optimum sensitivity S_{opt} via Equation (18); it is at this stage that laser power noise σ_{laser} becomes relevant, while as previously explained, detection noise σ_{det} can be considered practically negligible.

Step 3: Select a transparent solid with known index $n_o > n_r$ that can be shaped into a prism. Initially, avoid close-matching between the refractive indices of the front medium and the sample, so as to ensure substantial total transmittance. For the same reason, the number of reflections is initially set to $N = 1$.

Step 4: Given the light extinction spectrum of the sample, identify the laser wavelength that corresponds to the value of n_i which, when substituted to Equation (8), allows sensitivity to reach its optimal value S_{opt}.

Step 5: With all involved variables being determined, calculate the respective angular acceptance bandwidth A_{BW} using Equation (9); to sustain high total transmittance, select initially the external critical angle θ_c for grazing incidence.

Step 6: By use of the criteria shown in Equations (21) and (22), evaluate the feasibility of spatially-unresolved and spatially-resolved detection geometries. If found practical, the optimization process is complete and the setup fully drawn accordingly. Otherwise, go on to the next step:

Step 7: Repeat the process so as to increase A_{BW}, by selecting an optically denser transparent medium, a parallel plate with multiple reflections instead of a prism, and oblique incidence, in order to approach the operational limits $\{n_r/n_o,\ N,\ \theta_c\} \to \{1,\ \gg 1,\ 90°\}$. Ensure that the total transmittance is high enough to empower output light detection and the resulting plate length is small enough to comply with application's needs.

7. Further Discussion and Concluding Remarks

To demonstrate the susceptibility of the sensor's specifications to the various parameters involved, Table 1 presents results from the application of the proposed protocol to three hypothetical scenarios. Chosen values of variables remain within realistic ranges, being very tolerant in Case 1 and becoming more and more rigid as we move to Cases 2 and 3. Top rows in Table 1 group together noise-related parameters $\Delta T, \Delta\lambda$ and σ_{laser} (σ_{det} is considered negligible). The second set accounts for sample's optical properties, namely $n_r, n_i, dn_r/dT, dn_r/d\lambda$, while the third set incorporates information regarding the transparent medium and the prism/plate geometry, that is n_o, N and θ_c. Based on these values, acceptance bandwidth A_{BW} and ratios A_{BW}/θ_d are then evaluated. At the bottom of Table 1, corresponding values for the sensitivity S, optimal sensitivity S_{opt} and detection limit DL are given. In accordance with the protocol's guidelines, the sample's imaginary index n_i is always chosen such that sensitivity S, quantified via Equation (8), equals its optimal value S_{opt} which, in its own turn, is determined via Equation (18).

Several points of interests emerge from data in Table 1. Depending on the magnitude of ΔT and $\Delta\lambda$, the detection limit varies from 600 µRIU down 30 µRIU and sub-µRIU levels, as we move on from Case 1 via Case 2 to Case 3; DL reduction is accompanied by (i) increase in S_{opt} from 71 to 710 and 7100, (ii) decrease in n_i from 3×10^{-3} to 1.3×10^{-4} and 1×10^{-5}, (iii) narrowing of A_{BW} from 1.82° to 0.12° and 0.03°, respectively. Corresponding A_{BW}/θ_d values indicate that spatially-unresolved detection is possible with beam waists $w_o \geq 0.02$ mm, 0.37 mm and 1.25 mm, respectively, assuming for the sake of argument an operational wavelength in the 1 µm range. To meet these specifications, parameters $\{n_r/n_o, N, \theta_c\}$ changed from initial values $\{0.75, 1, 15°\}$ in Case 1, to $\{0.83, 2, 45°\}$ in Case 2 and $\{0.89, 4, 75°\}$ in Case 3; corresponding values for the prism/plate cut angle are $\alpha = 55.95°,\ 79.57°$ and 106.77°. As a final check, these changes cause no severe cutback to the overall plate transmittance, which always exceeds 50%, requiring, however, plate lengths as large as $L \approx 3$ cm in Case 2 and $L \approx 11$ cm in Case 3, for an assumed plate thickness $d = 0.5$ cm.

If such plate lengths are inappropriate, parameters $\{n_r/n_o, N, \theta_c\}$ can be kept constant to their initial values (i.e., $\{0.75, 1, 15°\}$). The detection limit would then be unaffected, but acceptance bandwidth would be reduced in Cases 2 and 3, such that spatially-unresolved detection would require beam waists $w_o \geq 2.5$ mm and 250 mm, respectively. Therefore, spatially-resolved detection would become a reasonable option in Case 2 and an inevitable choice in Case 3 for which, a maximum pixel diameter of 16 µm is specified, when plugging into the SRD criterion indicative values $w_o \approx 1$ mm and $w \approx 2$ mm.

Table 1. Results from the application of the optimization protocol to three hypothetical scenarios. Calculations assume $\delta_1 = \delta_2 = 1$, $M^2 = 1.2$ and $\sigma_{det} = 0$. Units: T in °C; λ in μ m; A_{BW} in degrees; w_o in mm; DL in μRIU. Other quantities are dimensionless. Sensor's linear range can be deduced from available data by use of Equation (16). Minimum useful signal (i.e., relative intensity change) at the detector amounts to $S \cdot DL \approx 4\%,\ 2\%$ and 0.4%, for Cases 1, 2 and 3, respectively.

Parameters	Case 1	Case 2	Case 3
ΔT	1	0.1	0.01
$\Delta\lambda$	10^{-3}	10^{-4}	10^{-5}
σ_{laser}	1%	0.5%	0.1%
n_r	1.5	1.5	1.5
n_i	3×10^{-3}	1.3×10^{-4}	1.0×10^{-5}
dn_r/dT	10^{-4}	5×10^{-5}	10^{-5}
$dn_r/d\lambda$	0.1	0.05	0.01
n_o	2	1.8	1.6
N	1	2	4
θ_c	15	45	75
A_{BW}	1.82	0.12	0.03
A_{BW}/θ_d	$41.5 \cdot w_o/\lambda$	$2.7 \cdot w_o/\lambda$	$0.8 \cdot w_o/\lambda$
$S = S_{opt}$	71	710	7100
DL	600	30	0.6

As a further practical demonstration on the relevance of our analysis to real-life applications, Figure 4 depicts the wavelength scaling of S and A_{BW} for two interfaces comprising water as rare medium and (i) calcium fluoride, (ii) standard $SF10$ glass, as front media. Water is chosen as an exemplary test medium since it is the main constituent of biofluids/tissues and a highly relevant medium for environmental sensing and quality control purposes. Calculations adopt values for the required optical constants (that is, the wavelength-dependent complex index of water and the wavelength-dependent real indices of CaF_2 and $SF10$, which can be considered transparent throughout the spectral range of interest) from references [39–41]. Within the near-infrared band 0.9 μm–1.6 μm, S and A_{BW} can be tuned by approximately two and three orders of magnitude, respectively, for the SF10/water interface and indicative values of $N = 1$, $\theta_c = 15°$. This behavior reflects primarily the absorption profile of water, which exhibits a minimum at 0.9 μm ($n_i \approx 4.5 \times 10^{-7}$) and a maximum at 1.46 μm ($n_i \approx 3.2 \times 10^{-4}$). Further tuning is possible by increasing the values of N, θ_c and simultaneously using CaF_2 as front medium, whose index matches better the real index of water, thus corresponding to larger values of n_r/n_o. Figure 4 reveals the heavy impact of laser wavelength on the sensor's specifications, an effect that does not apply only to water, but practically extends to all non-black, liquid or solid media that exhibit absorption profiles containing nearly-transparent regions, along with absorption peaks. Therefore, multipurpose critical angle refractometers, which are nowadays commercially available and typically equipped with just one or few single-wavelength lasers, would benefit significantly from exploiting tunable sources of coherent radiation, such as continuous-wave optical parametric oscillators [42].

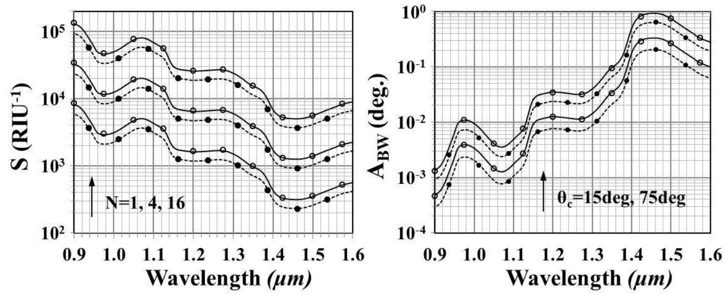

Figure 4. Sensitivity (**left**) and acceptance bandwidth (**right**), as a function of wavelength, for two indicative interfaces: CaF_2/H_2O (solid lines/open cicles) and $SF10/H_2O$ (dotted lines/black circles). Arrows indicate direction of increase in value of $N(= 1, 4, 16)$ and θ_c (=15 deg, 75 deg), respectively. Open circles correspond to exact values derived from signal-versus-incidence-angle plots, by use of Equations (2) and (6); solid lines are estimates from the empirical Equations (8) and (9).

To conclude, in this technical note we thoroughly examined the sensing properties of transparent/lossy interfaces. An empirical framework was developed to describe performance specifications of corresponding sensing geometries that exploit either a single reflection inside a prism, or multiple reflections inside a parallel plate. The dominant role of sample's loss was revealed and quantified through a trade-off between sensitivity on one hand and angular acceptance bandwidth on the other. These observations enabled the establishment of a generically applicable optimization's protocol that is based on two main realizations. First, a noise-dependent optimal value S_{opt} does exist, so that the quest for ever-increasing sensitivities is not just pointless, but also undesirable. Second, operating the sensing interface with $S = S_{opt}$ directly locks acceptance bandwidth A_{BW} to a calculable value, which then imposes definable conditions for the spatially-unresolved—or spatially-resolved—detection of the signal. The exemplary application of the proposed optimization protocol to three hypothetical scenarios revealed the critical dependence of sensor's specifications on the relevant optical and geometrical variables; this fact was further supported by calculations of the—widely varying—sensitivity S and acceptance bandwidth A_{BW}, as a function of wavelength, in the representative cases of the CaF_2/water and $SF10$/water interfaces. In this sense, the present note clarifies several design issues in the area of optical refractometry, relating to the pump source (e.g., choice of wavelength), the mounting medium (e.g., choice of prism material and geometry), as well as the detection stage (that is, spatially unresolved versus spatially resolved approach). We thus anticipate that our study will serve as a valuable tool for the realization of optimized CADR setups, which will push the limit of detection towards the sub-µRIU regime.

Author Contributions: Conceptualization, K.M.; methodology, S.K., P.G., D.T. and K.M.; validation, S.K., P.G. and K.M.; formal analysis, S.K., P.G. and K.M.; investigation, S.K., P.G., K.M.; writing–original draft preparation, K.M. and D.T.; writing–review and editing, K.M., D.T., P.G. and S.K.

Funding: This research received no external funding.

Conflicts of Interest: The authors declare no conflict of interest.

Appendix A. On the derivation of the empirical Equations (8) and (9)

Model building with data fitting was the basis for deriving the empirical Equations (8)—equivalently, (7)—and (9), which reproduce the sensitivity—or signal—and the angular acceptance bandwidth, respectively. The heuristic process involved the following steps:

(i). First, we attempted to identify the *independent variables* of the problem, out of a total number of nine initial variables, namely: $\{n_o,\ n_r,\ n_i,\ n_{air},\ \delta n_r,\ \delta n_i,\ N,\ \theta_c,\ \alpha\}$. To do so, we generated a large set of relative-intensity-change versus external-angle-of-incidence plots; from these plots, we were able to calculate "exact" values of $S = \left[\Delta I/I\right]_c/\delta$ and A_{BW} for various values of the nine starting variables. Close inspection of data revealed that S is practically independent on $\{n_{air},\ \theta_c,\ \alpha\}$, while A_{BW} is practically independent on $\{N,\ \alpha\}$. Inspired by the fact that the refractive indices of different media always enter in ratios in Fresnel equations, we were also able to establish that variables $\{n_o,\ n_r,\ n_i,\ n_{air},\ N\}$ are not independent, but can be reduced to a set of four variables, namely $\{n_r/n_o,\ n_i/n_o,\ n_{air}/n_o,\ N/n_o\}$. This realization was simply based on the observation that any changes in the values of $\{n_o,\ n_r,\ n_i,\ n_{air},\ N\}$ do not affect S and A_{BW}, provided that the ratios $\{n_r/n_o,\ n_i/n_o,\ n_{air}/n_o,\ N/n_o\}$ remain constant. Similarly, we noticed that variables $\{\delta n_r,\ \delta n_i\}$ can be reduced to only one independent variable, which is $\{\delta n_r/(\delta n_r + \delta n_i)\}$–or equivalently, $\{\delta n_r/\delta\}$. We thus concluded that independent variables are: $\{n_r/n_o,\ n_i/n_o,\ N/n_o,\ \delta n_r/\delta\}$ for S; $\{n_r/n_o,\ n_i/n_o,\ n_{air}/n_o,\ \delta n_r/\delta,\ \theta_c\}$ for A_{BW}.

(ii). Then, we attempted to capture the dependence of S and A_{BW} on each one of the independent variables, through least-square fitting of generated data. The employed functional forms (namely, exponentials, polynomials and rational functions, as shown in Equations (10)–(12)) are largely arbitrary, in the sense that they were chosen from a large set of different models, according to their simplicity and capability to best-agree with the generated data, rather than as a consequence of an underlying physical law. The only exception to this fully-empirical process accounts for the dependence of A_{BW} on $\{n_{air}/n_o,\ \theta_c\}$. In this case, we realized that the angular acceptance bandwidth physically originates from reflections at the interface between the prism (or plate) and the sample, and thus relates fundamentally with the internal angle θ_1. Throughout the main text, we use the external angle θ instead of θ_1 to define relevant quantities, since this is the actual angle of interest for the end-user. Therefore, we made the reasonable assumption that the derivative $[d\theta_1/d\theta]^{-1}$ should also be included as a term in the empirical equation for A_{BW}, in order to "translate" the internal angular bandwidth (in terms of θ_1) into an external one (in terms of θ). It is indeed this derivative that introduces the dependencies of A_{BW} on variables $\{n_{air}/n_o,\ \theta_c\}$ (see Equation (13)).

(iii). Finally, we generated additional data of S and A_{BW} (other than those used for fitting purposes), in order to establish the quality of the proposed empirical equations—Figure 3 is an exemplary demonstration of this test. We found out that the empirical model reproduces synthetic data with a typical accuracy of two significant digits which, as also claimed in the main text, is more than sufficient for evaluation purposes.

References

1. Bekmurzayeva, A.; Dukenbayev, K.; Shaimerdenova, M.; Bekniyazov, I.; Ayupova, T.; Sypabekova, M.; Molardi, C.; Tosi, D. Etched Fiber Bragg Grating Biosensor Functionalized with Aptamers for Detection of Thrombin. *Sensors* **2018**, *18*, 4298. [CrossRef] [PubMed]
2. Chiavaioli, F.; Gouveia, C.; Jorge, P.; Baldini, F. Towards a Uniform Metrological Assessment of Grating-Based Optical Fiber Sensors: From Refractometers to Biosensors. *Biosensors* **2017**, *7*, 23. [CrossRef] [PubMed]
3. Giannios, P.; Toutouzas, K.G.; Matiatou, M.; Stasinos, K.; Konstadoulakis, M.M.; Zografos, G.C.; Moutzouris, K. Visible to near-infrared refractive properties of freshly-excised human-liver tissues: marking hepatic malignancies. *Sci. Rep.* **2016**, *6*, 27910. [CrossRef] [PubMed]
4. Tan, R.; Yap, S.; Tan, Y.; Tjin, S.; Ibsen, M.; Yong, K.; Lai, W. Functionalized Fiber End Superstructure Fiber Bragg Grating Refractive Index Sensor for Heavy Metal Ion Detection. *Sensors* **2018**, *18*, 1821. [CrossRef] [PubMed]
5. Sequeira, F.; Duarte, D.; Bilro, L.; Rudnitskaya, A.; Pesavento, M.; Zeni, L.; Cennamo, N. Refractive Index Sensing with D-Shaped Plastic Optical Fibers for Chemical and Biochemical Applications. *Sensors* **2016**, *16*, 2119. [CrossRef] [PubMed]
6. Oelhafen, J.; Mayr, T.; Dorner, F.; Moutzouris, K.; Roths, J.; Drechsler, K. Fiber Optic Measurement System for Fresnel Reflection Sensing: Calibration, Uncertainty, and Exemplary Application in Temperature-Modulated Isothermal Polymer Curing. *J. Light. Technol.* **2018**, *36*, 939–945. [CrossRef]
7. Munap, D.H.A.; Bidin, N.; Islam, S.; Abdullah, M.; Marsin, F.M.; Yasin, M. Fiber Optic Displacement Sensor for Industrial Applications. *IEEE Sens. J.* **2015**, *15*, 4882–4887. [CrossRef]
8. Klinghammer, S.; Uhlig, T.; Patrovsky, F.; Böhm, M.; Schütt, J.; Pütz, N.; Baraban, L.; Eng, L.M.; Cuniberti, G. Plasmonic Biosensor Based on Vertical Arrays of Gold Nanoantennas. *ACS Sens.* **2018**, *3*, 1392–1400. [CrossRef] [PubMed]
9. Lal, S.; Link, S.; Halas, N.J. Nano-optics from sensing to waveguiding. *Nat. Photonics* **2007**, *1*, 641–648. [CrossRef]
10. Guerreiro, A.; Santos, D.F.; Baptista, J.M. New Trends in the Simulation of Nanosplasmonic Optical D-Type Fiber Sensors. *Sensors* **2019**, *19*, 1772.[CrossRef]
11. Kroh, C.; Wuchrer, R.; Steinke, N.; Guenther, M.; Gerlach, G.; Härtling, T. Hydrogel-Based Plasmonic Sensor Substrate for the Detection of Ethanol. *Sensors* **2019**, *19*, 1264. [CrossRef] [PubMed]
12. Xu, P.; Zheng, J.; Zhou, J.; Chen, Y.; Zou, C.; Majumdar, A. Multi-slot photonic crystal cavities for high-sensitivity refractive index sensing. *Opt. Express* **2019**, *27*, 3609. [CrossRef] [PubMed]
13. Qiao, Q.; Xia, J.; Lee, C.; Zhou, G. Applications of Photonic Crystal Nanobeam Cavities for Sensing. *Micromachines* **2018**, *9*, 541. [CrossRef] [PubMed]
14. Maurya, J.; François, A.; Prajapati, Y. Two-Dimensional Layered Nanomaterial-Based One-Dimensional Photonic Crystal Refractive Index Sensor. *Sensors* **2018**, *18*, 857. [CrossRef] [PubMed]

15. Wang, H.; Yan, X.; Li, S.; An, G.; Zhang, X. High Sensitivity Refractive Index Sensor Based on Dual-Core Photonic Crystal Fiber with Hexagonal Lattice. *Sensors* **2016**, *16*, 1655. [CrossRef] [PubMed]
16. Tsigaridas, G.N. A study on refractive index sensors based on optical micro-ring resonators. *Photonic Sens.* **2017**, *7*, 217–225. [CrossRef]
17. Arnold, S.; Khoshsima, M.; Teraoka, I.; Holler, S.; Vollmer, F. Shift of whispering-gallery modes in microspheres by protein adsorption. *Opt. Lett.* **2003**, *28*, 272. [CrossRef] [PubMed]
18. Zhu, H.; White, I.M.; Suter, J.D.; Dale, P.S.; Fan, X. Analysis of biomolecule detection with optofluidic ring resonator sensors. *Opt. Express* **2007**, *15*, 9139. [CrossRef]
19. Liu, W.; Yan, J.; Shi, Y. High sensitivity visible light refractive index sensor based on high order mode Si_3N_4 photonic crystal nanobeam cavity. *Opt. Express* **2017**, *25*, 31739. [CrossRef]
20. Tsigaridas, G.; Polyzos, D.; Ioannou, A.; Fakis, M.; Persephonis, P. Theoretical and experimental study of refractive index sensors based on etched fiber Bragg gratings. *Sens. Actuators A Phys.* **2014**, *209*, 9–15. [CrossRef]
21. Ahsani, V.; Ahmed, F.; Jun, M.; Bradley, C. Tapered Fiber-Optic Mach-Zehnder Interferometer for Ultra-High Sensitivity Measurement of Refractive Index. *Sensors* **2019**, *19*, 1652. [CrossRef] [PubMed]
22. Pugliese, D.; Konstantaki, M.; Konidakis, I.; Ceci-Ginistrelli, E.; Boetti, N.G.; Milanese, D.; Pissadakis, S. Bioresorbable optical fiber Bragg gratings. *Opt. Lett.* **2018**, *43*, 671. [CrossRef] [PubMed]
23. Apriyanto, H.; Ravet, G.; Bernal, O.D.; Cattoen, M.; Seat, H.C.; Chavagnac, V.; Surre, F.; Sharp, J.H. Comprehensive Modeling of Multimode Fiber Sensors for Refractive Index Measurement and Experimental Validation. *Sci. Rep.* **2018**, *8*, 5912. [CrossRef]
24. Wang, M.; Zhang, M.; Wang, Y.; Zhao, R.; Yan, S. Fano Resonance in an Asymmetric MIM Waveguide Structure and Its Application in a Refractive Index Nanosensor. *Sensors* **2019**, *19*, 791. [CrossRef] [PubMed]
25. Guo, Z.; Wen, K.; Hu, Q.; Lai, W.; Lin, J.; Fang, Y. Plasmonic Multichannel Refractive Index Sensor Based on Subwavelength Tangent-Ring Metal–Insulator–Metal Waveguide. *Sensors* **2018**, *18*, 1348. [CrossRef] [PubMed]
26. Hong, Y.S.; Cho, C.H.; Sung, H.K. Design Parameter Optimization of a Silicon-Based Grating Waveguide for Performance Improvement in Biochemical Sensor Application. *Sensors* **2018**, *18*, 781. [CrossRef] [PubMed]
27. Yan, S.; Zhang, M.; Zhao, X.; Zhang, Y.; Wang, J.; Jin, W. Refractive Index Sensor Based on a Metal–Insulator–Metal Waveguide Coupled with a Symmetric Structure. *Sensors* **2017**, *17*, 2879. [CrossRef] [PubMed]
28. Gong, X.; Ngai, T.; Wu, C. A portable, stable and precise laser differential refractometer. *Rev. Sci. Instrum.* **2013**, *84*, 114103. [CrossRef]
29. García-Valenzuela, A. Beam refraction and displacement in a differential refractometer with an absorbing sample. *Opt. Lett.* **2009**, *34*, 2192. [CrossRef]
30. Zilio, S.C. A simple method to measure critical angles for high-sensitivity differential refractometry. *Opt. Express* **2012**, *20*, 1862. [CrossRef]
31. McClimans, M.; LaPlante, C.; Bonner, D.; Bali, S. Real-time differential refractometry without interferometry at a sensitivity level of 10^{-6}. *Appl. Opt.* **2006**, *45*, 6477. [CrossRef] [PubMed]
32. Chen, J.; Guo, W.; Xia, M.; Li, W.; Yang, K. In situ measurement of seawater salinity with an optical refractometer based on total internal reflection method. *Opt. Express* **2018**, *26*, 25510. [CrossRef] [PubMed]
33. Sobral, H.; Peña-Gomar, M. Determination of the refractive index of glucose-ethanol-water mixtures using spectroscopic refractometry near the critical angle. *Appl. Opt.* **2015**, *54*, 8453. [CrossRef] [PubMed]
34. Morales-Luna, G.; García-Valenzuela, A. Viability and fundamental limits of critical-angle refractometry of turbid colloids. *Meas. Sci. Technol.* **2017**, *28*, 125203. [CrossRef]
35. Liu, H.; Ye, J.; Yang, K.; Xia, M.; Guo, W.; Li, W. Real part of refractive index measurement approach for absorbing liquid. *Appl. Opt.* **2015**, *54*, 6046. [CrossRef] [PubMed]
36. Lapsley, M.I.; Lin, S.C.S.; Mao, X.; Huang, T.J. An in-plane, variable optical attenuator using a fluid-based tunable reflective interface. *Appl. Phys. Lett.* **2009**, *95*, 083507. [CrossRef]
37. Weber, E.; Vellekoop, M.J. Optofluidic micro-sensors for the determination of liquid concentrations. *Lab Chip* **2012**, *12*, 3754. [CrossRef] [PubMed]
38. Zhang, L.; Zhang, Z.; Wang, Y.; Ye, M.; Fang, W.; Tong, L. Optofluidic refractive index sensor based on partial reflection. *Photonic Sens.* **2017**, *7*, 97–104. [CrossRef]

39. Kedenburg, S.; Vieweg, M.; Gissibl, T.; Giessen, H. Linear refractive index and absorption measurements of nonlinear optical liquids in the visible and near-infrared spectral region. *Opt. Mater. Express* **2012**, *2*, 1588. [CrossRef]
40. Daimon, M.; Masumura, A. High-accuracy measurements of the refractive index and its temperature coefficient of calcium fluoride in a wide wavelength range from 138 to 2326 nm. *Appl. Opt.* **2002**, *41*, 5275. [CrossRef]
41. Polyanskiy, M.N. Refractive Index Database. Available online: https://refractiveindex.info (accessed on 2 February 2019).
42. Dunn, M.H. Parametric Generation of Tunable Light from Continuous-Wave to Femtosecond Pulses. *Science* **1999**, *286*, 1513–1517. [CrossRef] [PubMed]